scientific reports

OPEN

FIB-fabrication of superconducting devices based on Bi_2Se_3 junctions

Rubén Gracia-Abad[1], Soraya Sangiao[1,2,3]✉, Geetha Balakrishnan[4] & José María De Teresa[1,3]✉

Recent advances in quantum technologies are highly influencing the current technological scenario. Hybrid devices combining superconductors and topological insulators represent an excellent opportunity to study the topological superconducting phase, which offers interesting features that might have significant implications in the development of quantum sensing and quantum computing. Furthermore, focused ion beam techniques, whose versatility enables to create sophisticated devices with high degree of customization, can enhance the creation of complex devices. Here, we develop a novel approach for creating single-crystal devices that is applied to the fabrication of superconducting devices based on topological insulator Bi_2Se_3 in a geometry characteristic of a superconducting quantum interference device. Characterization of these devices reveals that superconductivity is induced in our crystal and the supercurrent is modulated by applying an external magnetic field. These results open the way to tailoring the response of hybrid devices that combine superconductors and topological insulators by focused ion beam techniques.

Superconductor-based devices have settled the basis for the development of quantum technologies[1–3]. Specifically, the basic element of superconducting circuits is the Josephson Junction (JJ), which is found in most of the applications involving quantum sensing and quantum computing. For instance, two JJs are placed in parallel obtaining a Superconducting Quantum Interference Device (SQUID), a quantum sensor that represents the most sensitive tool for magnetic flux detection[4]. On the other hand, in quantum computing JJs are seen as non-linear inductors, which can be implemented for the fabrication of functional two-state qubits[5]. A new scenario has emerged in this field thanks to the incorporation of Topological Insulators (TIs) in superconducting devices. TIs are materials with an insulating bulk surrounded by topologically protected metallic surface states. The coupling of the superconductivity to the surface states of a TI by proximity effect gives rise to a topological superconducting phase[6,7], showing new exotic phenomena such as p-wave pairing, anomalous Josephson effect or the appearance of topologically protected Majorana bound states, which are of central interest in the development of fault-tolerant quantum computing, based on the braiding of these exotic excitations[8,9]. For these reasons, there is an ever-increasing interest in fabricating hybrid devices based on JJs that use a TI as a weak link, where this kind of phenomena can be studied[10]. Among TIs, Bi_2Se_3 has attracted much attention due to its simple surface band structure, its relatively large insulating gap of 0.3 eV, and its rather long phase-coherence length l_φ[11]. In this sense, Bi_2Se_3 represents an excellent platform for studying these new effects.

So far, Electron Beam Lithography (EBL) has represented the most widely employed technique in the fabrication of devices combining superconductors and TIs[12–14]. Nevertheless, the development of new and sophisticated superconducting devices can be boosted by the advantages of using Focused Ion Beam (FIB)-based techniques[15–17]. In contrast to other previously applied fabrication methods, FIB techniques avoid the use of chemical resists, and they can be implemented in a single step, reaching routinely a resolution below 100 nm. Additionally, the versatility of FIB-based techniques can be applied in the fabrication of devices with more complex geometries and unusual substrates. FIB relies on the acceleration and focusing of ions on a nanometric spot over a target substrate, enabling on the one hand, to remove material in a selected area, what is known as FIB patterning, and on the other hand, to deposit materials with a wide variety of properties, what is known as Focused Ion Beam Induced Deposition (FIBID). Interestingly, FIBID deposited W-C has demonstrated to be a type-II superconductor below $T_C \approx 4.5\ K$[18], being ideal for adding superconducting components during the fabrication of devices by FIB techniques and showing a high H_{C2} of $\approx 8\ T$[19].

FIB has already been successfully implemented in the fabrication of complex devices. For instance, Ga^+-FIB patterning of a thin Nb layer grown on a cantilever, has allowed the fabrication of a SQUID sensor on its tip to image small magnetic signals with high resolution[20,21]. Ga^+-FIB has also enabled the fabrication of superconducting devices out of single crystals such as SmFeAs(O, F)[22] or Sr_2RuO_4[23] allowing the investigation

[1]Instituto de Nanociencia y Materiales de Aragón (INMA), CSIC-Universidad de Zaragoza, Zaragoza 50009, Spain. [2]Laboratorio de Microscopías Avanzadas (LMA), Universidad de Zaragoza, Zaragoza 50018, Spain. [3]Departamento de Física de la Materia Condensada, Universidad de Zaragoza, Zaragoza 50009, Spain. [4]Department of Physics, University of Warwick, Coventry CV4 7AL, UK. ✉email: sangiao@unizar.es; deteresa@unizar.es

of their intrinsic properties, or the realization of planar JJs based on high-T_C superconductors such as BSSCO[24] or YBCO[25,26]. Indeed, junctions with an extremely high resolution of 10 nm have been fabricated on YBCO with He^+-FIB using low doses[27,28]. Besides, Ga^+-FIB has been used for the fabrication of much more complex systems such as superconducting microwave resonators[29,30], useful in qubit control. In this case, Ne^+-FIB has also been applied, yielding better resolution[31].

Apart from FIB patterning, the use of Ga^+-FIBID has also been applied to fabricate other types of superconducting devices, such as JJ arrays of NbC[32] or W-C nanoSQUIDs with Dayem-bridge-type geometry[33], with the potential of being grown on a cantilever for magnetic imaging. FIBID deposits have been frequently employed in order to induce superconductivity in other materials, paving the way for the fabrication of S-N-S junctions, i.e., a normal metal N as a weak link sandwiched between two superconducting contacts S. This technique has been successfully applied to the combination of W-C deposited by FIBID with different materials such as graphene[34], Bi[35], Au[36] or even TIs such as Bi_2Se_3[37]. Indeed, this also demonstrates the utility of this technique for investigating Majorana physics[13,14,38]. However, the application of S-TI-S junctions in the fabrication of SQUIDs with a conventional geometry for quantum sensing has not been fully explored.

Here in, we put forward the combination of FIB patterning and FIBID for the fabrication of a superconducting device with a conventional SQUID geometry containing JJs that use the TI Bi_2Se_3 as a weak link. The use of FIB-based techniques offers the ability to customize the size and shape of the different parts of the device and to further modify the different elements, allowing us to explore the properties of the device. First, we introduce a novel FIB-based fabrication procedure that starts with the fabrication of a Bi_2Se_3 single-crystal device, on top of which the superconducting W-C contacts will be grown. Second, we will show the electrical characterization of two of our superconducting devices and how the superconductivity is induced on the Bi_2Se_3 single crystal, giving rise to a magnetic response explained by the formation of a coherent supercurrent in our devices.

Results

Fabrication of Bi_2Se_3-based superconducting devices

The complete fabrication process to prepare superconducting devices starting from a Bi_2Se_3 single crystal can be divided into two main steps: In the first one, a Bi_2Se_3 device is fabricated out of the single crystal by following a procedure consisting of an adaptation of a Transmission Electron Microscopy (TEM) lamella fabrication process[15,39], in which a micrometer-sized sample is extracted from a Bi_2Se_3 single crystal and transferred onto a prefabricated Si/SiO_2 chip with gold electric pads, this step is illustrated schematically in Fig. 1g. In the second part, the device is provided with superconducting properties by growing a W-C deposit on top and further modifying it.

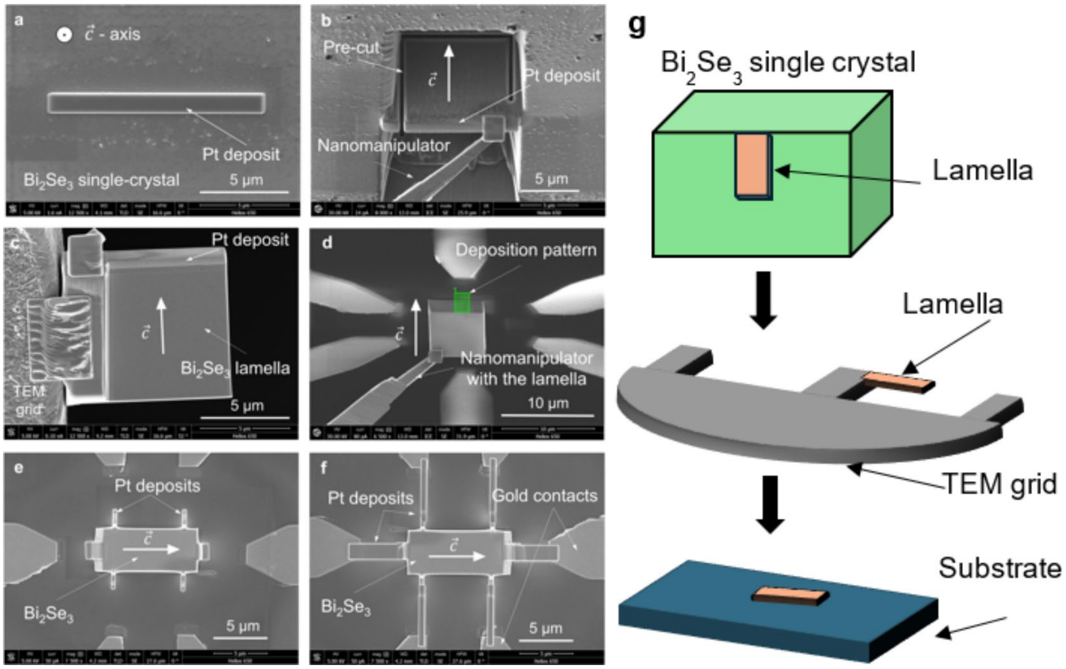

Fig. 1. SEM micrographs of the fabrication process of the single-crystal device: (a) Protective Pt deposit grown by FIBID. (b) Pre-cut lamella attached to the Omniprobe. (c) TEM grid with the lamella after the cleaning process. (d) Landing of the lamella in the region between the gold pads of the chips. Green rectangle represents the pattern of the Pt deposit by FIBID. (e) First part of the Pt leads grown by FIBID at $\alpha = 0^\circ$. (f) Final functional Bi_2Se_3 single-crystal device. (g) 3D scheme of the fabrication process, from the starting point in which we have a Bi_2Se_3 single crystal (fig. a) to the lamella landed on the final substrate (fig. e).

Fabrication of Bi_2Se_3 single-crystal devices

The first step begins with the extraction of a coarse rectangular slab out of the single crystal. From now on, this slab will be referred to as lamella. In order to protect the Bi_2Se_3 material close to the surface, a Pt-C deposit is grown by FIBID on the area where the lamella is extracted from (Fig. 1a). The FIB is used at $\alpha = 52^\circ$ to create trenches on both sides of the Pt-C deposit. The complete process is carried out in such a way that in the final device the current is injected along the direction parallel to the c-axis, which is now parallel to the crystal slab. Hence, the longitudinal dimension of the device will be determined by the depth of the trenches. After this, the lamella is pre-cut with the FIB at $\alpha = 0^\circ$ leaving it connected to the bulk crystal through just a small region on one side (Fig. 1b).

To complete the extraction, an Omniprobe nanomanipulator is introduced in the process chamber and the lamella is attached to it. The lamella is completely freed from the crystal by cutting the remaining region that connects it to the crystal. Then, it is withdrawn and attached to the TEM sample grid (Fig. 1c). This grid acts as an intermediary, as it will be shown later. While the lamella is resting in the grid, a cleaning process at low ion beam current is applied on both faces in order to thin it down to the desired thickness and to remove the material damaged during the coarse extraction process. A thickness about $1\,\mu m$ is chosen. Now, the lamella has to be transferred onto the chip, but before this, a reorientation is required in order to lay its largest faces parallel to the chip surface. That can be attained simply by opening the process chamber and laying flat the TEM grid on which the lamella is held. After that, the nanomanipulator is used once again to transfer the lamella onto the region between the electric contacts of the prefabricated chip is such a way that the c-axis is aligned parallel to the longitudinal direction through which the current will travel (Fig. 1d).

After the landing, the sample is electrically connected to the gold pads by FIBID-deposited Pt leads. These leads are grown in two steps. A first deposit is grown at $\alpha = 0^\circ$ in order to overcome the height (thickness) of the crystal (see Fig. 1e). With this value of α, the face of the lamella where the deposit has to be grown is directly exposed to the ion beam. The lead is then finished by growing a second deposit at $\alpha = 52^\circ$ going from the first deposit up to the gold pad. The same process is applied for the remaining leads, rotating the stage after each one to obtain the right orientation between the sample and the ion beam.

Once the leads are completed, a functional Bi_2Se_3 device is achieved (Fig. 1f).

Fabrication of the superconducting devices

In the second step of the process, the Bi_2Se_3 single-crystal device will be turned into a superconducting device for which an 80-nm thick W-C deposit is grown on top by FIBID (Fig. 2a). The shape of the deposit consists of a central longitudinal strip and two transverse pads that cover the entire width of the crystal up to the Pt transverse voltage leads in such a way that the voltage drop along the W-C deposit can be measured.

Next, a wide junction is fabricated by cutting the center of the device along the entire width of the W-C deposit in order to remove the W-C deposit but not the single-crystal underneath in such a way that the Bi_2Se_3 beneath acts as a weak link between the two sides of the W-C deposit (Fig. 2b). This step requires soft working conditions so that the milling of the Bi_2Se_3 underneath is minimized.

Finally, a hole is fabricated in the center of the junction by FIB milling, providing the device with its final SQUID-like geometry (Fig. 2c). The material in the hole is removed down to the Si/SiO_2 substrate, so undesired shunt resistors are avoided. For the same reason, the remaining Bi_2Se_3 single crystal on the sides of the W-C deposit are removed by FIB milling. After this, a functional superconducting device is obtained (Fig. 2d).

Electrical characterization of the devices

The electrical characterization of the devices was carried out at two different stages of the process. A first electrical characterization of each device was performed after completing the manufacturing process of the Bi_2Se_3 single-crystal device. Then, once the complete fabrication of the superconducting device is finished, a second electrical characterization step was carried out.

Electrical characterization of Bi_2Se_3 single-crystal devices

Figure 3 shows the results for samples labelled as A, B and C. The longitudinal resistivity versus temperature curves presents a metallic behaviour ($d\rho / dT > 0$) for all of them (Fig. 3a), which indicates the presence of a bulk Fermi surface contributing to the transport. This bulk contribution is dominated by a single channel formed by electrons, as indicated by the linear dependence with negative slope in Hall resistivity ρ_{xy} versus magnetic field curve (Fig. 3c). The n-type doping is commonly found in Bi_2Se_3 and is attributed to the natural formation of Se vacancies that populate the bulk conduction band with electrons[40], hindering the identification of the topological surface states. The Hall measurements enable to determine the carrier density that is in the order of $10^{19}\,cm^{-3}$ and the mobility that ranges between 100 and $300\,cm^2V^{-1}s^{-1}$. Finally, the longitudinal magnetoresistance ρ_{xx} increases with magnetic field due to the contribution of the Lorentz Force, presenting a classical behaviour (Fig. 3b).

Electrical characterization of the superconducting devices

Samples B and C were further turned into superconducting devices by following the procedure described in the previous section. In sample B (Fig. 4a), the Bi_2Se_3 material on the sides of the W-C deposit are still present, whereas it was removed by FIB milling in sample C (Fig. 4b).

Figure 5a and b show the temperature dependence of the resistance and the $I-V$ characteristic at 0.8 K of both samples, respectively. The drop to zero in the temperature dependence of the resistance indicates a superconducting transition induced by proximity effect in the Bi_2Se_3 crystal. Sample B presents a single well-defined transition with critical parameters $T_C = 4.2\,K$ and $I_C = 42.5\,\mu A$, whereas sample C presents a double

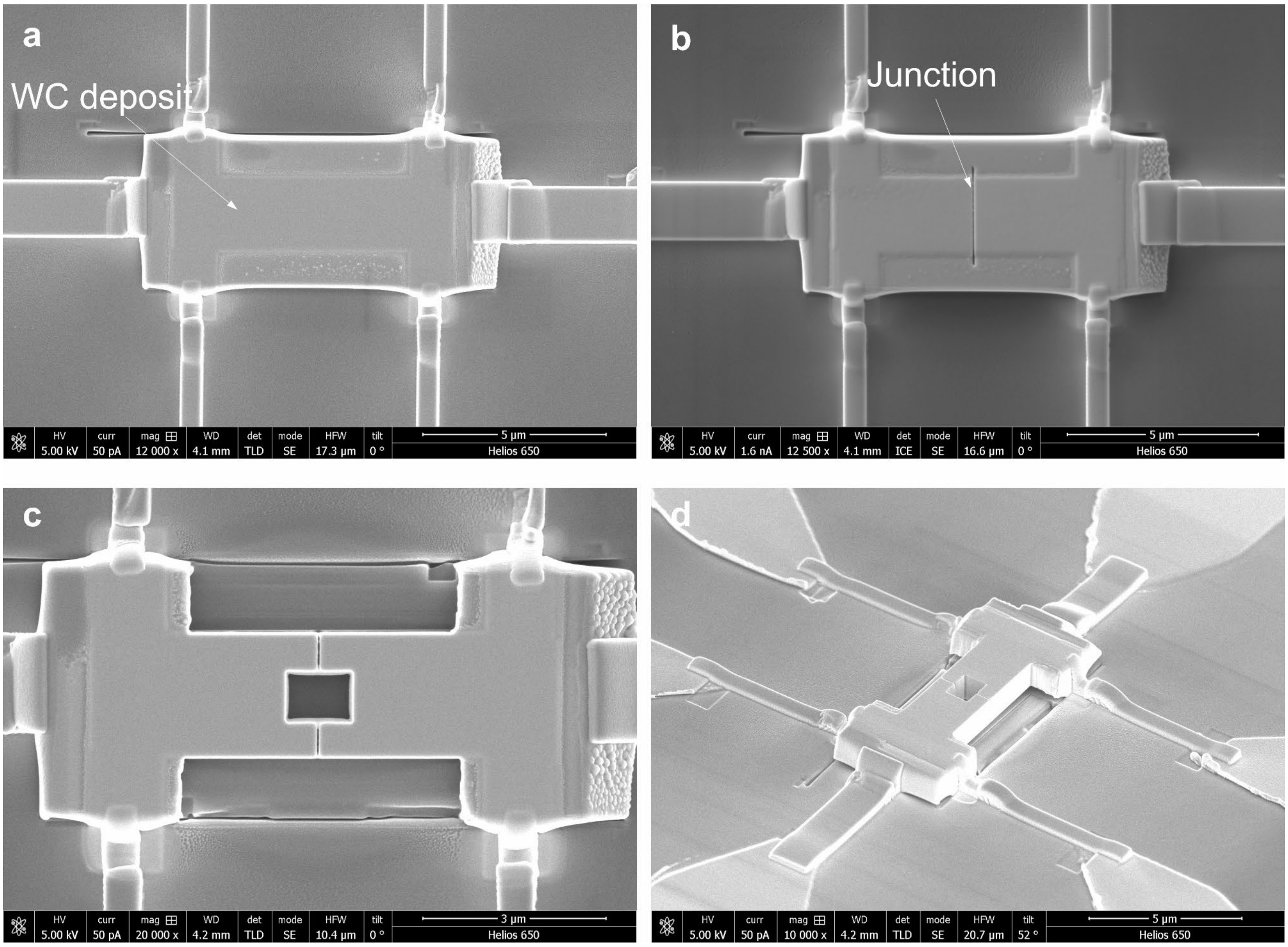

Fig. 2. SEM micrographs of the fabrication process of the superconducting device: (a) W-C superconducting deposit by FIBID placed on the central region of the single-crystal device. (b) Fabrication of a wide junction by cutting the W-C deposit along its entire width by FIB patterning. (c) Fabrication of a hole by FIB in the center of the junction by FIB milling. (d) Final device with SQUID-like geometry.

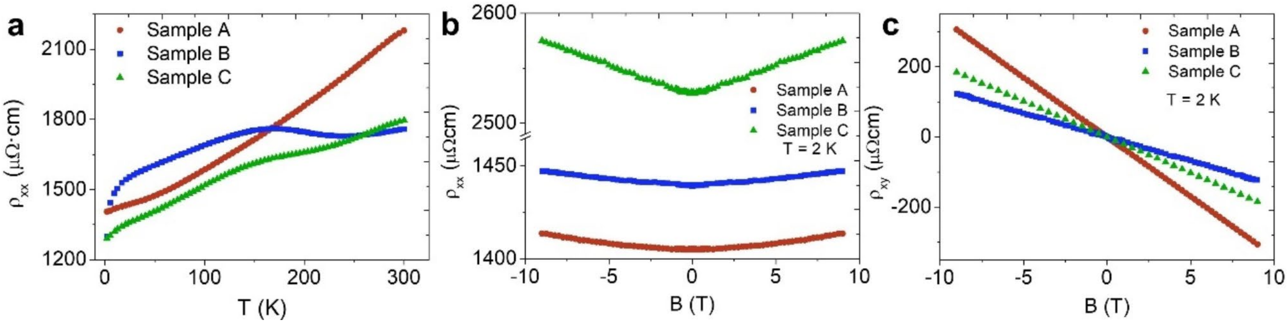

Fig. 3. Electrical characterization of three different Bi_2Se_3 single-crystal devices: (a) Longitudinal resistivity versus temperature. (b) Longitudinal magnetoresistance measured at 2 *K*. (c) Magnetic field dependence of the Hall resistivity measured at 2 *K*.

transition with parameters $T_{C1} = 3.4\ K$and $T_{C2} = 4.6\ K$ in temperature and $I_{C1} = 6.8\ \mu\ A$and $I_{C2} = 42.5\ \mu\ A$ in current. The critical parameters with higher values are attributed to the W-C deposits, whereas the parameters with lower values are attributed to the Bi_2Se_3 junction whose superconducting properties are expected to be weaker than those of the deposit.

I-V characteristics measured at 0.8 *K* for samples B and C at different magnetic fields applied perpendicular to the plane of the devices are shown in Fig. 6a and b, respectively. A very clear modulation of the measured *I-V*

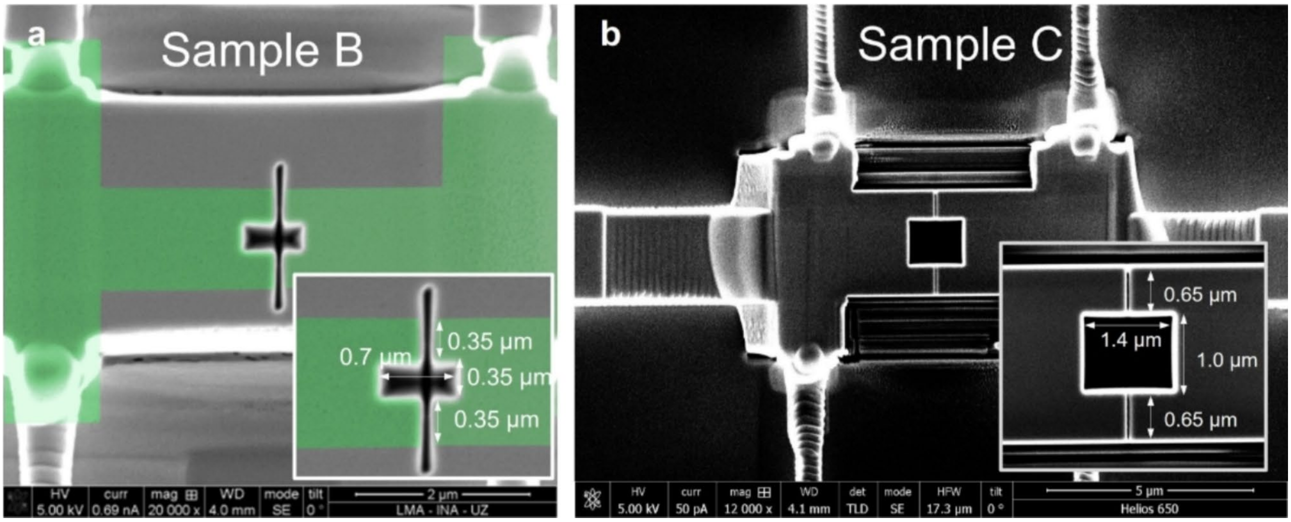

Fig. 4. SEM micrographs of the superconducting devices based on Bi_2Se_3 single crystals corresponding to samples B (a) and C (b) previously discussed. The W-C deposit in sample B is indicated by the green shaded region, whereas in sample C, the deposit covers the entire width. Insets show a magnified view of the corresponding holes with the precise determination of their dimensions.

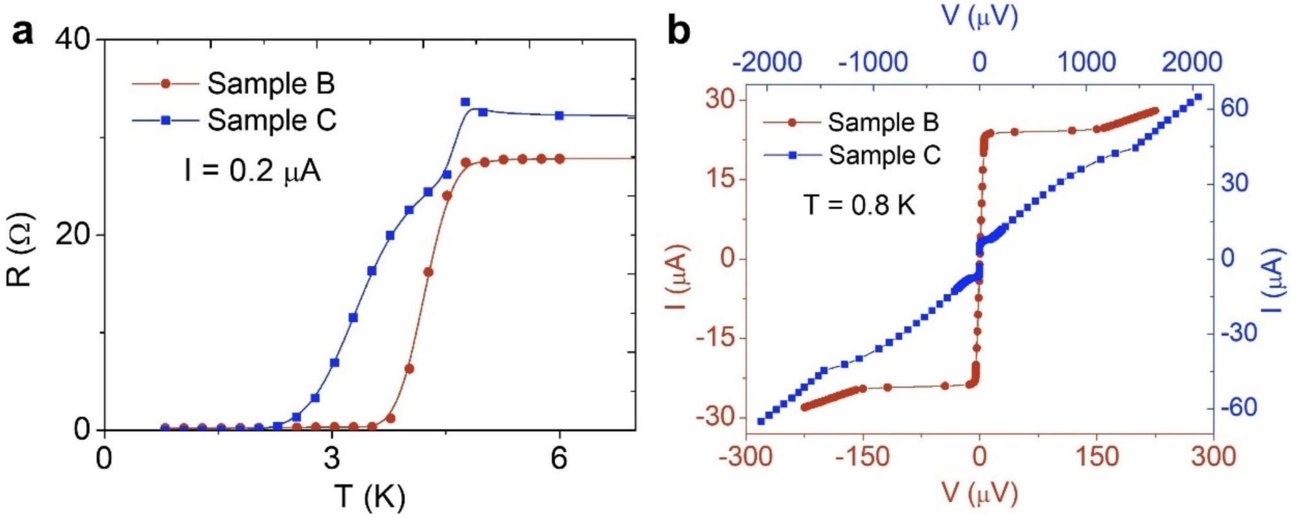

Fig. 5. Resistance versus temperature curves measured at $I = 0.2\ \mu A$. (b) I-V characteristics measured at $T = 0.8\ K$.

characteristics is observed as a function of the applied magnetic field in both samples. This modulation is further manifested in the magnetic field dependence of the voltage measured at fixed current for current values close to the critical one (Fig. 6c and d), where it is superimposed to a background in both cases. The curves were measured at a current at which the modulation observed in the voltage is the highest. The presence of the background is likely due to magnetoresistance effects in the crystal and to the system exiting the superconducting state as the magnetic field is increased reaching its critical value. The modulation in sample B shows a conventional behaviour that is difficult to fit to a SQUID model due to the presence of the background and to the low number of oscillations that exist within the range of field where the voltage modulates. However, the few minima can be located (see blue arrows in Fig. 6b) and a periodicity of $(71 \pm 2)\,Oe$ is found, corresponding to an effective area of $0.28\,\mu\,m^2$, well in agreement with the geometrical area ($0.245\,\mu\,m^2$, as can be observed in Fig. 4a).

On the other hand, sample C presents an unconventional behaviour with several interesting features. First, the modulation of the voltage survives up to relatively high magnetic fields of nearly $1\,T$, presenting high values in the low-field region reaching nearly 100% at $\approx\ 0.07\,T$ (see Fig. 6e). This large modulation is an interesting characteristic for sensing applications. Second, the behaviour cannot be explained through a single oscillatory component, but the complex pattern seems to be produced by at least two of them: A quicker one with a shorter

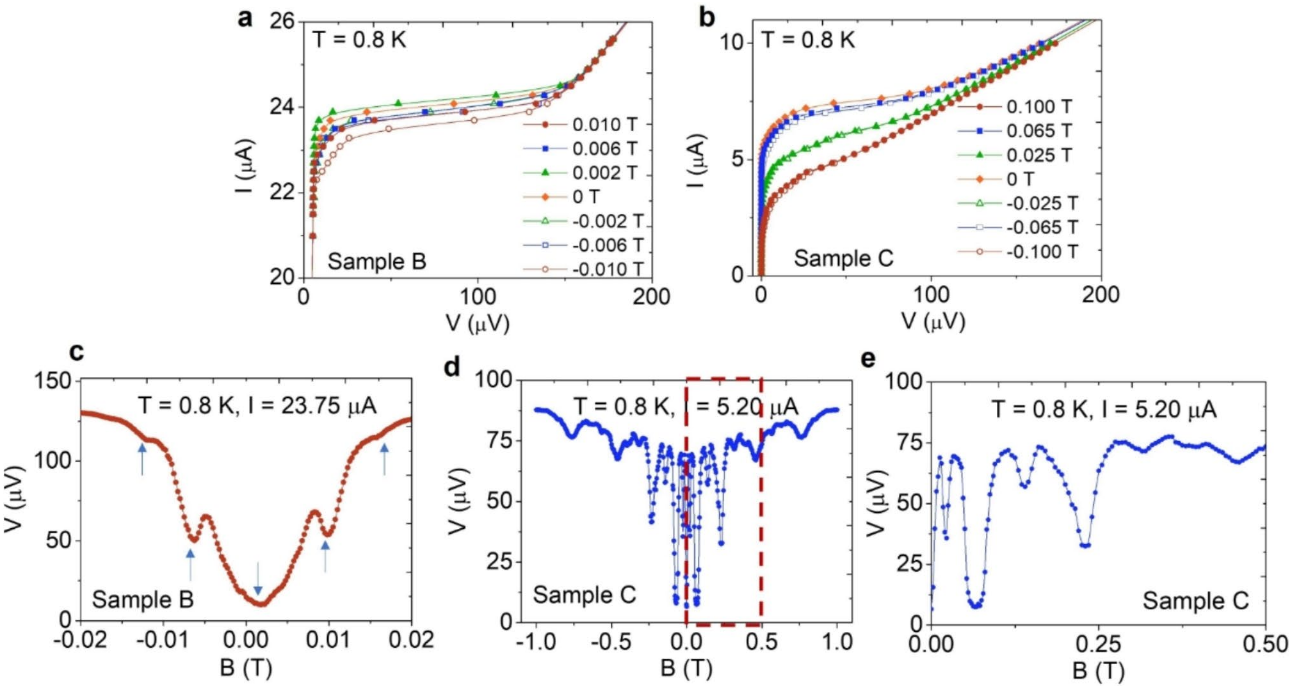

Fig. 6. *I*-*V* characteristics at different magnetic fields for sample B (a) and C (b). (c) Magnetic field dependence of the voltage at $0.8\ K$ and $23.75\ \mu\ A$ for sample B. Blue arrows indicate the position of the voltage minima. (d) Magnetic field dependence of the voltage at $0.8\ K$ and $5.20\ \mu\ A$ for sample C. (e) Zoom into the dashed region indicated in (d).

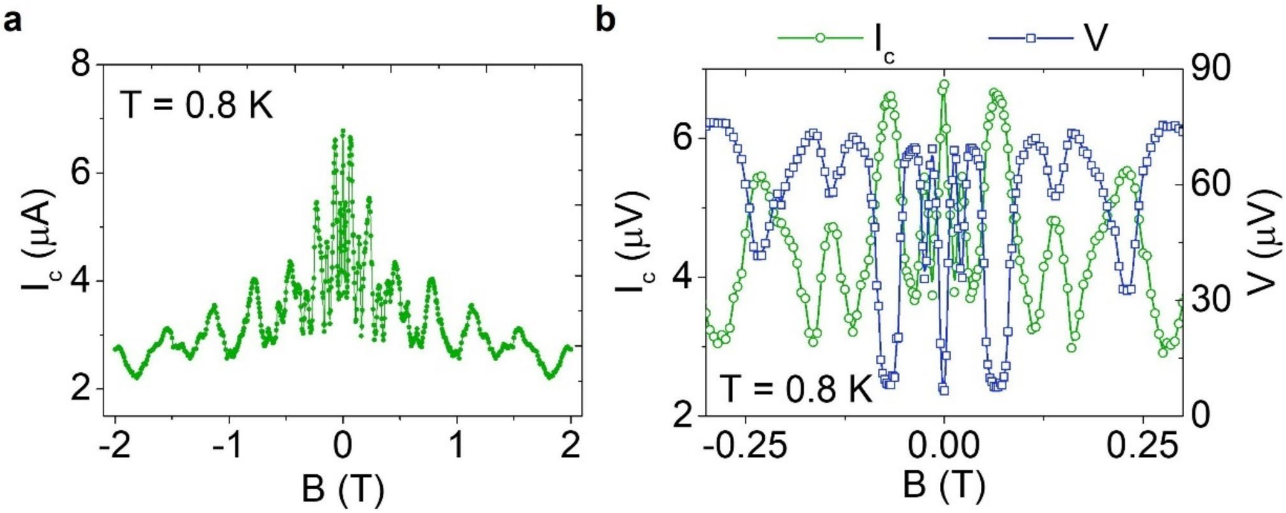

Fig. 7. (a) Magnetic field dependence of the critical current I_C at $T = 0.8\ K$ for sample C. (b) Magnetic field dependence of the voltage and the critical current in the low magnetic field region at $T = 0.8\ K$.

period that dominates in the low field region and is slowly suppressed as the field is increased and a slower one with a large period that survives up to higher magnetic field values.

Figure 7a shows the magnetic field modulation of the critical current I_C, which presents the same behaviour as the voltage, with its minima and maxima corresponding to maxima and minima in the voltage, respectively, and reproducing the same features (Fig. 7b). This confirms the consistency of the measurements.

As explained above, a single SQUID component is not able to describe our results. As a first hypothesis, a parallel contribution of the SQUID loop together with the two individual junctions was considered. This has been observed in several previous works when the dimensions of the loop and the dimensions of the junctions are comparable and their corresponding periods are present in the modulation[14]. In order to test this, one of the junctions was removed by the FIB and the device was measured again, the SEM micrograph of sample

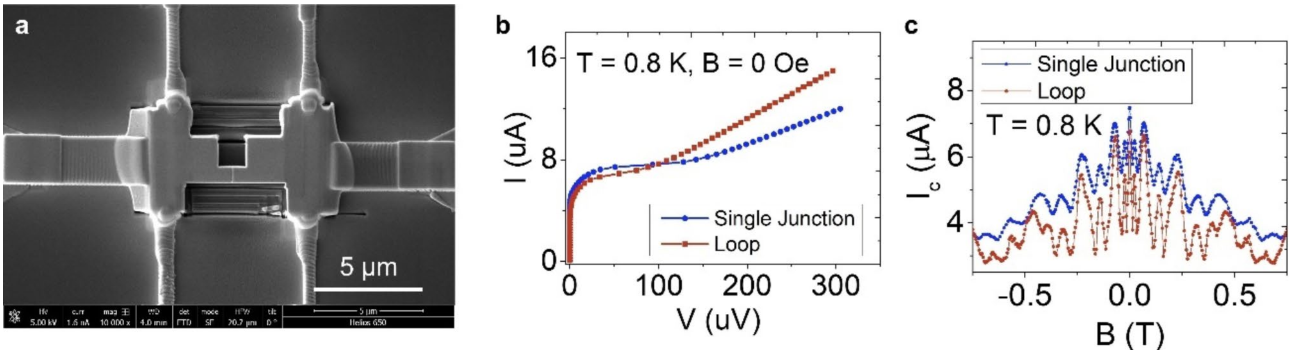

Fig. 8. (a) SEM micrograph of sample C after removing one of the junctions by FIB. (b) I-V characteristics before (Loop) and after (Single junction) the removal of one of the junctions measured at $T = 0.8\ K$. (c) Magnetic field dependence of I_C at $T = 0.8\ K$ before (Loop) and after (Single junction) the removal of one of the junctions.

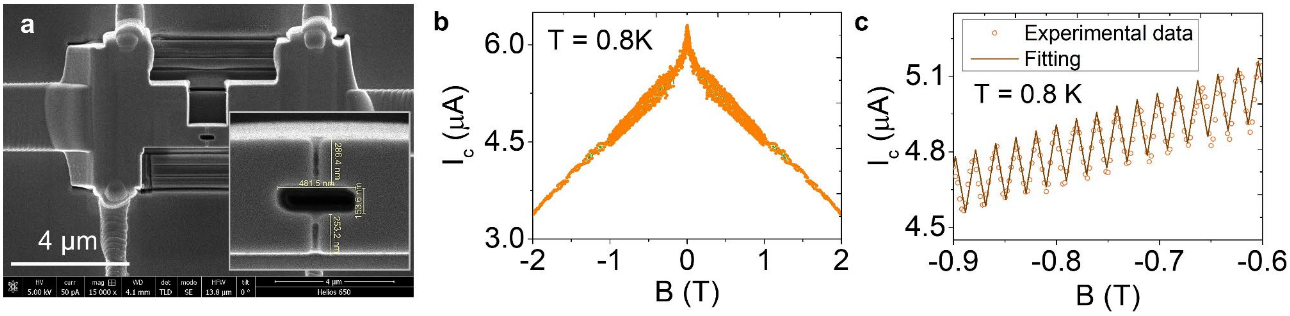

Fig. 9. SEM micrograph of sample C after fabricating a hole in the center of the remaining junction. (b) Magnetic field dependence of the critical current measured at $T = 0.8\ K$ in the magnetic field range from $-2\ T$ to $2\ T$. (b) Magnetic field dependence of the critical current measured at $T = 0.8\ K$ plotted from from $-0.9\ T$ to -0.6 T with fitting to model described by Eq. 1.

C after this modification being displayed in Fig. 8a. The critical parameters barely change (Fig. 8b) and the complex pattern in the magnetic field modulation is still present (Fig. 8c), indicating that no significant changes have been produced after the modification. According to this, the supercurrent in the previous experiments was travelling mainly across the remaining junction, and the removed junction was not playing any significant role. Both results, the unchanged magnetic field modulation after removal of one junction compared to the full loop and the intricate single junction pattern we have obtained, indicate that the critical current density is not homogeneous along the junction.

As a last modification step, a hole was made by FIB in the center of the remaining junction, creating a new SQUID geometry, as shown in Fig. 9. The electrical properties of the resulting device were then investigated. The behaviour was now drastically changed, and the complex behaviour observed before was replaced by a conventional behaviour with much lower critical current modulation, which indicated a high screening parameter in the device. Particularly, a modulation depth of $\Delta I_C/I_0$ of $\approx\ 0.04$ is found in the range between $0.5\ T$ and $1\ T$. This data could be fitted by a standard SQUID model. Specifically, a model for high screening parameter β_L was applied[41], with I_C as a function of the magnetic flux Φ given by:

$$I_C(\Phi) = 2I_0 - \frac{2\,|\Phi - n\Phi_0|}{L} + A\Phi \tag{1}$$

With $n - \frac{1}{2} \leq \frac{\Phi}{\Phi_0} \leq n + \frac{1}{2}$. Φ_0 is the magnetic flux quantum, L is the inductance of the SQUID, I_0 is the critical current of the individual junctions, and $A\Phi$ is a linear term added to account for the linear background. This model enabled to determine the periodicity of the oscillation as $(196.0 \pm\ 0.1)\,Oe$, which provides an effective area of $(0.1020 \pm\ 0.0001)\,\mu\,m^2$. This area is 56% larger that the geometrical area of $0.065\ \mu\,m^2$, which is likely due to flux-focusing effect in the W-C contacts[42]. On the other hand, an I_0 of $(3.20 \pm\ 0.01)\ \mu\,A$ and an L of $(8.8 \pm\ 0.3)\ nH$ are obtained. This provides a value of β_L of $28.1 \pm\ 1.0$ in good agreement with the low critical current modulation depth found in these last measurements.

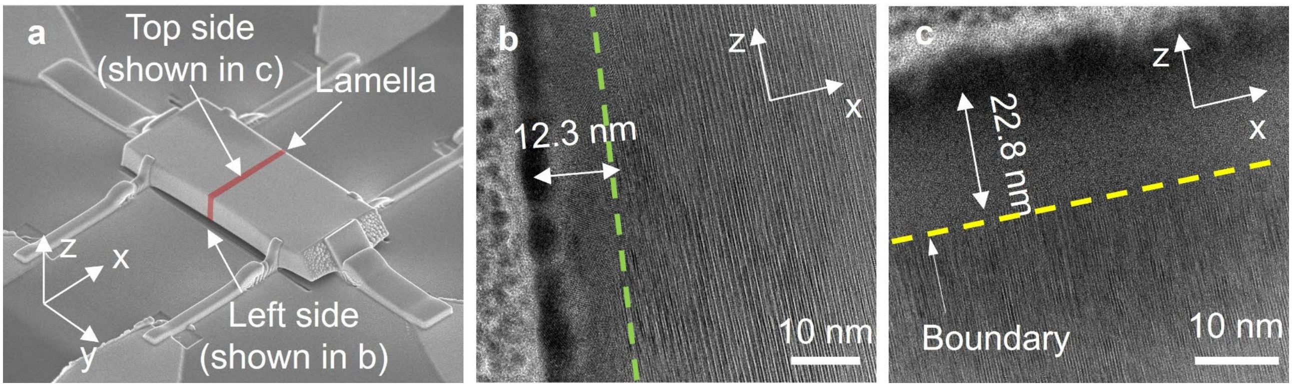

Fig. 10. (a) SEM micrograph of the resulting Bi_2Se_3 device indicating the regions from which the lamella was extracted with the zones corresponding to micrographs (b) and (c). TEM micrographs of the left side (b) and top side (c) of the transverse area of the resulting Bi_2Se_3 device. Dashed lines in (b) and (c) indicate the boundaries between the amorphous and crystalline phases of the Bi_2Se_3 crystal.

Discussion

The results observed in the previous section in sample C before the last modification step cannot be described by a standard model for SQUIDs or JJs, in which the magnetic field produces a modulation of the voltage and critical current described by a single oscillatory component with a well-defined period. This evidences the necessity to look for new contributions in the coherent transport across the junctions that could explain the complex behaviour in this device. At this point the role of topologically protected states existing in the Bi_2Se_3 crystal is considered. Once the superconducting W-C contact has been grown on top, the current is expected to be confined mainly in the region right beneath the deposit, at a distance over which the superconductivity is induced when the system is in the superconducting state, as well as, during the transition. This leads to a more significant role of the surface of the Bi_2Se_3 crystal in the overall transport than before the deposition of the superconducting contact.

The structural characterization of one of the fabricated devices right before the deposition of the W-C contact on top shows the formation of an amorphous shell that surrounds the crystalline Bi_2Se_3 structure, which extends over a distance between 10 *nm* and 30 *nm* depending on the region of the lamella (as can be observed in TEM micrographs shown in Fig. 10). This amorphous region has been created due to the ion irradiation applied during the fabrication process in the lamella extraction, and it is later enhanced in the fabrication of the junction. Despite the damage created on the surface and potential Ga doping[43], a well-defined amorphous/crystalline (A/C) interface appears where topological states can emerge, as discussed hereafter.

The appearance of topological states at an A/C boundary created by the irradiation through Ga^+-FIB has been recently demonstrated in the TI Sb_2Te_3[44]. Above a certain irradiation dose, the amorphized material becomes topologically trivial, which produces an interface with the crystalline material at which the topology changes, inducing the appearance of topological states at that interface. Sb_2Te_3 and Bi_2Se_3 belong to the same family of tetradymite chalcogenide TIs and are expected to undergo similar consequences after ion irradiation in terms of structural damage.

After the last fabrication step, the ion irradiation applied for the fabrication of the hole in the remaining junction would destroy the coherent channels of the bulk and surface states, leaving behind a residual conductance across the new junctions that produces the conventional behaviour observed next.

Conclusions and outlook

In this work we have developed a new approach based on the use of FIB related techniques, such as FIB patterning and FIBID, to fabricate functional superconducting devices based on single-crystal Bi_2Se_3 combined with FIBID-grown W-C. The use of FIB has provided plenty of versatility in the design of the device, resulting in the fabrication of functional TI devices with customized geometry and extra fabrication steps have allowed us to explore the electrical properties of these devices in a geometry characteristic of a SQUID and of a JJ.

The electrical characterization has given evidence for superconductivity induced in the topological insulator Bi_2Se_3 by proximity effect in two different devices (samples B and C). This magnetic response has shown high modulation depth both, in the critical current and the output voltage, that survives up to high magnetic fields of 1 *T* for sample C.

Magnetic field modulation in sample C presented an unconventional behaviour manifested through intricate patterns in the critical current and in the output voltage, with the contribution of different coherent channels providing larger and shorter interference components that were difficult to isolate. As a feasible explanation, we have considered the presence of both contributions, the individual JJs and the SQUID loop. This hypothesis has been tested by removing one of the junctions and very similar behaviour was observed afterwards, indicating that only the remaining junction was actually playing a relevant role in the superconducting transport. Finally, the unconventional behaviour disappeared after the last fabrication step in which a loop was drilled by FIB in the remaining junction. This final fabrication step led to a more conventional behaviour in which the magnetic response presented a lower modulation depth created by a single oscillatory component that could be analysed through standard models of SQUID.

This study opens up the possibility for the design of future hybrid devices combining TIs and superconductors. On the other hand, further research could combine Ga^+-FIB with FIBs based on other ionic species such as He^+ and Ne^+ for the fabrication of the JJs. He^+-FIB would provide higher resolution and lower milling rates, allowing even more precise control of the milling process that should be translated into a better ultimate performance of the superconducting devices.

Methods

High quality Bi_2Se_3 single crystals were synthesized by the modified Bridgman method[45], which involves a static growth setup where the ampoule containing the polycrystalline version of the desired material is placed vertically in a box furnace. The temperature of the furnace is slowly increased up to the melting temperature of the material and kept long enough to allow complete melt and diffusion of all the components in the ampoule. Finally, the furnace temperature is slowly reduced allowing crystallization of the melt to take place. The crystallinity was ascertained by x-ray Laue diffraction, whereas the topological nature was validated by angle-resolved photoemission spectroscopy. The only well-known crystallographic direction corresponds to the out-of-plane c-axis that points in the direction normal to the plane of the crystal.

Electronic devices were prepared starting from a Bi_2Se_3 single crystal. For this purpose, the capabilities of a Dual Beam Helios Nanolab 650 from Thermofisher (Hillsboro, OR, USA) were exploited. This equipment combines a vertical field emission electron column with a 52° -tilted Ga+-based FIB column, both with a maximum acceleration voltage of 30 kV, which allows one to simultaneously fabricate and image the process. Both beams intersect at the eucentric point, which is placed 4.15 nm below the pole of the electron column. The sample is mounted in a stage that provides translational, rotational and tilting degrees of freedom enabling to properly orientate the sample respect to the beams. The tilting angle, defined as the angle between the electron column and the direction normal to the plane of the stage, is denoted as α and is set during the fabrication of the devices to two main values: $\alpha = 0^\circ$ and $\alpha = 52^\circ$, with normal incidence of the electron beam and of the ion beam, respectively.

The electrical characterization of the devices was carried out in a Physical Properties Measurement System from Quantum Design (California, US), covering temperatures down to 0.8 K and perpendicular magnetic fields up to 9 T.

For structural characterization, some lamellas of the devices were observed in a Titan Cube 60–300 TEM from Thermofisher (Hillsboro, OR, USA) with high-resolution TEM capabilities. This equipment allows the irradiation of the samples with high-energy electrons up to $300\,keV$ and incorporates a spherical aberration corrector that improves the resolution down to 1 Å.

Data availability

All data analyzed and presented in the current study are available from the corresponding authors on reasonable request.

Received: 4 April 2024; Accepted: 7 October 2024

References

1. Devoret, M. H. & Schoelkopf, R. J. Superconducting circuits for Quantum Information: an Outlook. *Sci. (80-).* **339**, 1169–1174 (2013).
2. Degen, C. L., Reinhard, F. & Cappellaro, P. Quantum sensing. *Rev. Mod. Phys.* **89**, 035002 (2017).
3. Wendin, G. Quantum information processing with superconducting circuits: a review. *Rep. Prog Phys.* **80**, 106001 (2017).
4. José Martínez-Pérez, M., Koelle, D. & NanoSQUIDs Basics & recent advances. *Phys. Sci. Rev.* **2**, 20175001 (2017).
5. Wendin, G. & Shumeiko, V. S. Quantum bits with Josephson junctions (review article). *Low Temp. Phys.* **33**, 724–744 (2007).
6. Fu, L. & Kane, C. L. Superconducting Proximity Effect and Majorana Fermions at the Surface of a topological insulator. *Phys. Rev. Lett.* **100**, 096407 (2008).
7. Sato, M. & Ando, Y. Topological superconductors: a review. *Rep. Prog Phys.* **80**, 076501 (2017).
8. Kitaev, A. Anyons in an exactly solved model and beyond. *Ann. Phys. (N Y).* **321**, 2–111 (2006).
9. Sarma, S., Das, Freedman, M. & Nayak, C. Majorana zero modes and topological quantum computation. *Npj Quantum Inf.* **1**, 15001 (2015).
10. Schüffelgen, P. et al. Selective area growth and stencil lithography for in situ fabricated quantum devices. *Nat. Nanotechnol.* **14**, 825–831 (2019).
11. Gracia-Abad, R. et al. Omnipresence of weak antilocalization (WAL) in Bi_2Se_3 Thin films: a review on its origin. *Nanomaterials.* **11**, 1077 (2021).
12. Sacépé, B. et al. Gate-tuned normal and superconducting transport at the surface of a topological insulator. *Nat. Commun.* **2**, 575 (2011).
13. Williams, J. R. et al. Unconventional Josephson Effect in Hybrid Superconductor-Topological Insulator devices. *Phys. Rev. Lett.* **109**, 056803 (2012).
14. Kurter, C., Finck, A. D. K., Hor, Y. S. & Van Harlingen, D. J. Evidence for an anomalous current–phase relation in topological insulator Josephson junctions. *Nat. Commun.* **6**, 7130 (2015).
15. Moll, P. J. W. Focused Ion Beam Microstructuring of Quantum Matter. *Annu. Rev. Condens. Matter Phys.* **9**, 147–162 (2018).
16. De Teresa, J. M. Nanoscale direct-write fabrication of superconducting devices for application in quantum technologies. *Mater. Quantum Technol.* **3**, 013001 (2023).
17. Höflich, K. et al. Roadmap for focused ion beam technologies. *Appl. Phys. Rev.* **10**, 041311 (2023).
18. Orús, P., Sigloch, F., Sangiao, S. & De Teresa, J. M. Superconducting materials and devices grown by Focused Ion and Electron Beam Induced Deposition. *Nanomaterials.* **12**, 1367 (2022).
19. Sadki, E. S., Ooi, S. & Hirata, K. Focused-ion-beam-induced deposition of superconducting nanowires. *Appl. Phys. Lett.* **85**, 6206–6208 (2004).

20. Wyss, M. et al. Magnetic, thermal, and Topographic Imaging with a nanometer-scale SQUID-On-Lever scanning probe. *Phys. Rev. Appl.* **17**, 034002 (2022).
21. Marchiori, E. et al. Magnetic imaging of superconducting qubit devices with scanning SQUID-on-tip. *Appl. Phys. Lett.* **121**, 052601 (2022).
22. Moll, P. J. W. et al. High magnetic-field scales and critical currents in SmFeAs(o, F) crystals. *Nat. Mater.* **9**, 628–633 (2010).
23. Yasui, Y. et al. Spontaneous emergence of Josephson junctions in homogeneous rings of single-crystal Sr_2RuO_4. *Npj Quantum Mater.* **5**, 21 (2020).
24. Kim, S. J., Latyshev, Y. I. & Yamashita, T. Submicron stacked-junction fabrication from $Bi_2Sr_2CaCu_2O_{8+\delta}$ whiskers by focused-ion-beam etching. *Appl. Phys. Lett.* **74**, 1156–1158 (1999).
25. Kang, D. J. et al. Realization and properties of $YBa_2Cu_3O_{7-\delta}$ Josephson junctions by metal masked ion damage technique. *Appl. Phys. Lett.* **80**, 814–816 (2002).
26. Testa, G. et al. Submicron $YBa_2Cu_3O_{7-x}$ bicrystal grain boundary junctions by focused ion beam. *Supercond Sci. Technol.* **17**, 287–290 (2004).
27. Cybart, S. A. et al. Nano Josephson superconducting tunnel junctions in $YBa_2Cu_3O_{7-\delta}$ directly patterned with a focused Helium ion beam. *Nat. Nanotechnol.* **10**, 598–602 (2015).
28. Müller, B. et al. Josephson junctions and SQUIDs created by Focused Helium-Ion-Beam irradiation of $YBa_2Cu_3O_7$. *Phys. Rev. Appl.* **11**, 044082 (2019).
29. Jenkins, M. D. et al. Nanoscale constrictions in superconducting coplanar waveguide resonators. *Appl. Phys. Lett.* **105**, 162601 (2014).
30. Gimeno, I. et al. Enhanced molecular spin-photon coupling at Superconducting nanoconstrictions. *ACS Nano.* **14**, 8707–8715 (2020).
31. Kennedy, O. W. et al. Tunable Nb Superconducting Resonator based on a Constriction Nano-SQUID fabricated with a Ne focused Ion Beam. *Phys. Rev. Appl.* **11**, 014006 (2019).
32. Porrati, F. et al. Highly-packed proximity-coupled DC-Josephson Junction arrays by a direct-write Approach. *Adv. Funct. Mater.* **32**, 2203889 (2022).
33. Sigloch, F., Sangiao, S., Orús, P. & de Teresa, J. M. Direct-write of tungsten-carbide nanoSQUIDs based on focused ion beam induced deposition. *Nanoscale Adv.* **4**, 4628–4634 (2022).
34. Shailos, A. et al. Proximity effect and multiple Andreev reflections in few-layer graphene. *Europhys. Lett.* **79**, 57008 (2007).
35. Sangiao, S., Casado, L., Morellón, L., Ibarra, M. R. & De Teresa, J. M. Proximity-induced superconductivity in bismuth nanostripes. *J. Phys. D Appl. Phys.* **50**, 02 (2017).
36. Wang, J. et al. Proximity-Induced Superconductivity in nanowires: Minigap State and Differential Magnetoresistance oscillations. *Phys. Rev. Lett.* **102**, 247003 (2009).
37. Bhattacharyya, B., Awana, V. P. S., Senguttuvan, T. D., Ojha, V. N. & Husale, S. Proximity-induced supercurrent through topological insulator based nanowires for quantum computation studies. *Sci. Rep.* **8**, 17237 (2018).
38. Cho, S. et al. Symmetry protected Josephson supercurrents in three-dimensional topological insulators. *Nat. Commun.* **4**, 1689 (2013).
39. Mayer, J., Giannuzzi, L., Kamino, T. & Michael, J. T. E. M. Sample Preparation and FIB-Induced damage. *MRS Bull.* **32**, 400–407 (2007).
40. Scanlon, D. O. et al. Controlling Bulk Conductivity in Topological insulators: key role of Anti-site defects. *Adv. Mater.* **24**, 2154–2158 (2012).
41. Clarke, J. & Braginski, A. I. *The SQUID Handbook* (Wiley, 2004). https://doi.org/10.1002/3527603646
42. Brandt, E. H. Thin superconductors and SQUIDs in perpendicular magnetic field. *Phys. Rev. B.* **72**, 024529 (2005).
43. Kudriashov, A. et al. Revealing intrinsic superconductivity of the Nb/BiSbTe$_2$Se Interface. *Adv. Funct. Mater.* **32**, 2209853 (2022).
44. Bake, A. et al. Top-down patterning of topological surface and edge states using a focused ion beam. *Nat. Commun.* **14**, 1693 (2023).
45. Biswas, D., Thakur, S., Balakrishnan, G. & Maiti, K. Exceptional surface and bulk electronic structures in a topological insulator, Bi_2Se_3. *Sci. Rep.* **5**, 17351 (2015).

Acknowledgements

Authors acknowledge grants PID2020-112914RB-I00, PID2023-1464510B-I00 and CEX2023-001286-S funded by MCIN/AEI/10.13039/501100011033, CSIC, through Research Platform PTI-001 and also Gobierno de Aragón through the doctoral fellowship (R. G. A.) and the grant number E13_23R, with European Social Funds (Construyendo Europa desde Aragón). The following networking projects are acknowledged: Spanish Nanolito (RED2022-1634096-T) and COST-FIT4NANO (action CA19140). Authors acknowledge the Laboratory for Advanced Microscopies (LMA) and the Institute of Nanoscience and Materials of Aragón (INMA) from CSIC-Universidad de Zaragoza for offering access to their instruments and expertise. Technical support by the LMA technicians at Universidad de Zaragoza is acknowledged, particularly thank to L. Casado for her assistance with the nanomanipulation procedures. Authors acknowledge also the Physical Measurements Service from Servicio General de Apoyo a la Investigación (SAI) - University of Zaragoza. The work at the University of Warwick was supported by EPSRC, UK through Grant EP/T005963/1.

Author contributions

R.G.A. performed the device fabrication and the magnetotransport experiments and analyzed the data. R.G.A. and S.S. wrote the first draft of the manuscript. G.B. performed the growth of the Bi_2Se_3 single crystal and carried out its structural characterization. S.S. and J.M.D.T. got the funding, conceived the experiments, supervised the research and contributed to the data interpretation and the writing of the manuscript. All authors reviewed the manuscript.

Declarations

Competing interests

The authors declare no competing interests.

Additional information

Correspondence and requests for materials should be addressed to S.S. or J.M.T.

Reprints and permissions information is available at www.nature.com/reprints.

Publisher's note Springer Nature remains neutral with regard to jurisdictional claims in published maps and institutional affiliations.

Open Access This article is licensed under a Creative Commons Attribution-NonCommercial-NoDerivatives 4.0 International License, which permits any non-commercial use, sharing, distribution and reproduction in any medium or format, as long as you give appropriate credit to the original author(s) and the source, provide a link to the Creative Commons licence, and indicate if you modified the licensed material. You do not have permission under this licence to share adapted material derived from this article or parts of it. The images or other third party material in this article are included in the article's Creative Commons licence, unless indicated otherwise in a credit line to the material. If material is not included in the article's Creative Commons licence and your intended use is not permitted by statutory regulation or exceeds the permitted use, you will need to obtain permission directly from the copyright holder. To view a copy of this licence, visit http://creativecommons.org/licenses/by-nc-nd/4.0/.

© The Author(s) 2024